TUDelft

Delft University of Technology

Palladium-PTFE Metal-Polymer Nanocomposite Film Produced by Cosputtering for Hydrogen Sensing Applications

Bannenberg, Lars Johannes; Krishnan, Gopi; Boshuizen, Bart; Schreuders, Herman

Important note
To cite this publication, please use the final published version (if applicable).
Please check the document version above.

Article

Palladium-PTFE Metal−Polymer Nanocomposite Film Produced by Cosputtering for Hydrogen Sensing Applications

Published as part of ACS Applied Energy Materials special issue "Metal−Hydrogen Systems".

Lars Johannes Bannenberg,* Gopi Krishnan, Bart Boshuizen, and Herman Schreuders

Read Online

ACCESS | 📊 Metrics & More | 📰 Article Recommendations | 🔲 Supporting Information

ABSTRACT: Here, we show that we can synthesize free-standing palladium nanoparticles with a size of about 5 nm embedded in a fluorinated polymer matrix using magnetron codeposition and a subsequent annealing step. Indeed, we deposit with magnetron sputtering at the same time PTFE and Pd, and a subsequent thermal annealing step under a hydrogen atmosphere ensures agglomeration of the Pd atoms into small nanoparticles. This scalable vapor-based method allows deposition on all kinds of surfaces, including substrates and optical fibers. Using a combination of transmission electron microscopy, grazing-incidence diffraction, neutron and X-ray reflectometry, and X-ray photoelectron spectroscopy, we characterize the nanocomposite films and the palladium particles inside. These palladium nanoparticles could have a variety of applications in catalysis, hydrogen compressors, and optical hydrogen sensors. For the later application, we show using optical transmission measurements that the nanoparticles can reversibly absorb hydrogen, having well-defined steps in optical transmission when the hydrogen pressure is changed. Owing to their small size, the polymer matrix, and high surface-to-volume ratio, the nanoparticles show subsecond response times to changes in hydrogen concentration.

KEYWORDS: metal hydrides, nanocomposite film, palladium, PTFE, optical hydrogen sensing
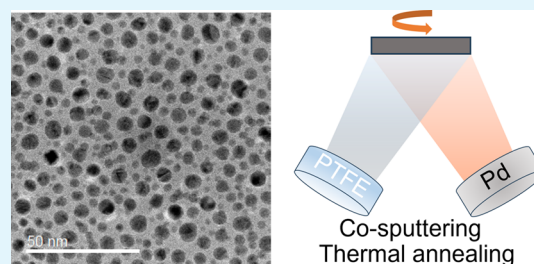
1. INTRODUCTION

Palladium nanoparticles have attracted a continuous stream of attention. Palladium serves as the archetype metal-hydride system and has been subject to a large body of fundamental studies in which the interaction of Pd and hydrogen and the influence of size, shape, and strain are thereon.[1−7] In part, the attractiveness of Pd stems from the fact that palladium possesses both the ability to catalyze the hydrogen dissociation reaction in which molecular hydrogen is converted to atomic hydrogen and the ability to absorb relatively large quantities of hydrogen at moderate hydrogen pressures. This enables its applications in catalysis, hydrogen storage, hydrogen compressors, and hydrogen sensors.

For bulk materials, the palladium−hydrogen phase diagram consists of two phases. When bulk PdH_x is exposed to relatively low hydrogen pressures at room temperature, a solid solution between hydrogen and palladium forms for low hydrogen-to-metal ratios of $x \lesssim 0.02$, the so-called α-PdH_x phase. For larger values of x, obtained when the pressure exceeds the plateau pressure, attractive hydrogen−hydrogen interactions become dominant, and a high-hydrogen concentration β-phase nucleates with $x \approx 0.6$. For even higher hydrogen pressures, the hydrogen-to-metal ratio x in the β-phase further increases with increasing pressure. In both the α and β phases, hydrogen atoms occupy the octahedral sites of the face-centered cubic Pd lattice. As the

nucleation of the β phase is accompanied by a volume increase of roughly 7%, substantial mechanical work is required. As such, this implies a substantial energy barrier to be present in the system, and accordingly, hysteresis is seen in the system with a much larger absorption than desorption pressure. For temperatures larger than the critical temperature $T_C \approx 290−300$ °C, a single phase is observed and the transition is coherent rather than incoherent in nature.[8,9]

The thermodynamics of nanosized palladium are substantially different from its bulk counterparts (see, e.g., refs 1−7). As a result of the large lattice distortion needed to accommodate the hydrogen atoms, the phase transition is inherently size- and shape-dependent. Indeed, differences in surface-to-volume ratio, stress/strain effects resulting, for example, from interactions with a support, and the presence of defects can strongly affect the thermodynamics of the system. Generally speaking, for the case of palladium nanoparticles, smaller particles exhibit a lower
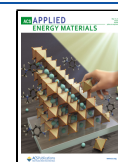
hydrogenation pressure than larger particles and a substantially larger solubility of hydrogen within the α phase.

One of the applications of palladium is as an (optical) hydrogen sensing material.[10−15] In this application, the ability of palladium to absorb hydrogen, and in turn change its optical properties, is used to create a hydrogen sensor.[14,16−23] In such a sensor, palladium is, for example, produced as a thin film using magnetron sputtering and, e.g., the optical transmission, reflectivity, or (localized)-surface plasmon resonances are probed, which all change when palladium absorbs hydrogen as it is exposed to sufficiently high partial hydrogen pressures. As such, one can, when the material has been calibrated as a sensor, deduce the hydrogen concentration based on the measured optical properties. In this light, the attractiveness of palladium as a sensing material stems from the fact that it can readily absorb hydrogen at room temperature without the need of an additional catalyst, that the change of the optical properties is relatively large, and that the sensor works for a relatively modest partial hydrogen pressure sensing range of $10^1 \lesssim P_{H_2} \lesssim 10^4$ Pa. Nevertheless, it has some severe problems: it is prone to blistering and microcracking, making the sensor unstable; it features long response times; and the sensing range is relatively modest. Moreover, it suffers from hysteresis as a result of the incoherent α-to-β-PdH$_x$ transition, making the optical response to an increasing hydrogen pressure different from that of a decreasing hydrogen pressure. As such, many alternative metal hydride sensing materials have been developed, noteworthy palladium-alloys and tantalum-based hydrogen sensing materials.[19−21,24−26]

Another approach is to exploit the fact that palladium, as a tiny nanoparticle (<10 nm), has profoundly different properties from bulk or thin film palladium. For hydrogen sensing applications, this potentially allows an abundance of advantages in terms of hysteresis, sensing range, long-term durability, and response time. Hysteresis may be drastically reduced, and the larger solubility of hydrogen in the α-phase, in which the hydrogen-to-metal ratio is gradually increased with increasing hydrogen pressure, would facilitate a much larger partial hydrogen pressure window in which hydrogen can be quantified. Moreover, as stress release in small nanoparticles can be much easily accomplished than in clamped thin films, the possibility of microcrack formations and delamination is drastically reduced, improving the long-term durability of the material. Last, the small nanoparticles have a large surface-to-volume ratio and short diffusion paths, allowing fast (de)hydrogenation kinetics and thus short response times. These kinetics could be even further enhanced when the particles could be embedded in a PTFE layer, a material known to be able to boost the hydrogenation kinetics and provide protection against unwanted chemical species.[27−29]

Creating polymer−nanoparticle composite films in a scalable manner is an art on its own. In the context of palladium-nanocomposite films for hydrogen sensing applications, colloidal synthesis was used to create a Pd-PMMA nanocomposite material,[30] and a continuous-flow synthesis resulted in the formation of Pd nanoparticles in an amorphous fluorinated polymer[31] with relatively thick thicknesses ($\sim$100 μm). Furthermore, Mg nanoparticles have been synthesized in a PMMA matrix where PMMA also provided protection against humidity and oxygen.[32,33] Alternatively, magnetron sputtering has been used in the literature to create metallic nanoparticles in a polymer matrix.[34−36] If it were possible to use magnetron

sputtering to synthesize palladium nanoparticles, this method would have plenty of advantages: Magnetron sputtering is a well-established method that is used commercially, has modest deposition times, is solvent-free, and can be used to deposit on almost any kind of surface, thus including optical fibers. The latter is especially important for hydrogen sensing applications, as many proposed sensor designs involve the use of optical fibers.[16,22,23]

Here, we report a simple, scalable two-step method to create a palladium-PTFE composite thin films by codeposition of Pd and PTFE with magnetron sputtering and subsequent thermal annealing. Using transmission electron microscopy (TEM) and grazing-incidence X-ray diffraction (GIXRD), X-ray and neutron reflectometry, and X-ray photoelectron spectroscopy, we show that when sputtered in the correct ratio, we create a nanocomposite film with Pd nanoparticles with a size of around 5 nm inside a fluorinated polymer matrix. Optical transmission measurements indicate that the composite film shows well-defined optical changes when exposed to hydrogen and that the material can efficiently absorb hydrogen with subsecond response times.

2. EXPERIMENTAL SECTION

2.1. Sample Fabrication. The films are produced with codeposition of Pd and PTFE using radio frequency (rf) magnetron sputtering in combination with an annealing step. The depositions are performed ultrahigh vacuum chamber (AJA Int.) with a base pressure of $P < 10^{-6}$ Pa in 0.3 Pa of Ar and a sample-to-target distance of 150 mm. A schematic of the sputter geometry can be found in Figure S1. The layers are deposited on either silicon nitride TEM grids (PELCO 15 nm thick with 9 apertures of each 0.1×0.1 mm^2, Ted Pella, Inc., Redding, California, United States of America) for TEM studies, $0.5 \times 10 \times 10$ mm^2 fused quartz substrates with a surface roughness < 0.4 nm (Mateck GmbH, Jülich, Germany) for X-ray diffraction, X-ray reflectometry and optical measurements, and on fused quartz substrates with a diameter of 76.2 mm (3 in), a thickness of 3.0 mm, and a surface roughness <0.5 nm for neutron reflectometry measurements (Esco Optics inc., Oak Ridge, New Jersey, United States of America). The sputter target has a diameter of 50.1 mm (2 in), the Pd target has a purity of at least 99.9% and a thickness of 6.35 mm (Mateck GmbH, Jülich, Germany), and the PTFE target has a thickness of 5 mm and a density of 2.2 g cm^{-1} (FP303200, Goodfellow Cambridge Ltd., Huntington, United Kingdom).

Films with in total four different compositions of Pd and PTFE were fabricated, i.e., Pd+PTFE, Pd25PTFE75, Pd50PTFE50, and Pd75PTFE25, where the ratios correspond to the volume of the individual materials. These nominal compositions/thicknesses were determined by XRR on individually sputtered films of approximately 40 nm of Pd and approximately 40 nm of PTFE. On the basis of these measurements, the deposition rate at each sputter power/tilt angle could be determined. The Pd+PTFE film is a film made by sequentially sputtering 30 nm Pd and 30 nm PTFE. The Pd75PTFE25, Pd50PTFE50, and Pd25PTFE75 films were fabricated by simultaneously sputtering Pd and PTFE at different ratios by varying the deposition powers and tilt angle of the gun. The thickness was scaled in such a way that the amount of Pd atoms in each sample is approximately the same, i.e., the Pd25PTFE50 is three times thicker than the Pd75PTFE25 film. The deposition power, time, rates, and tilt of the gun for each of the samples are provided in Table 1. During the deposition, the samples were rotated at 20 rotations per minute to obtain a homogeneous composition and thickness. Subsequent annealing of the samples was performed by exposing them to T = 200 °C for 4 days, during which we exposed them to 8 cycles of hydrogen with 15 logarithmically spaced steps in pressure varying between P_{H_2} = 110 Pa and $P_{H_2} = 10^6$ Pa. These steps were equal in duration across time. The Pd25PTFE75 sample for neutron reflectometry measurements was

Table 1. Deposition Conditions of the Films Made[a]

	nominal thickness (nm)	power Pd (W)	power PTFE (W)	deposition time (min: s)	tilt Pd gun (°)
Pd + PTFE	30 + 30	16.5	70	9:16	5
Pd75PTFE25	40	16.5	70	9:16	5
Pd50PTFE50	60	5.5	70	27:47	5
Pd25PTFE75	120	4.2	70	83:00	0

[a]The Pd+PTFE film is a film made by sequentially sputtering 30 nm Pd and 30 nm PTFE. The Pd75PTFE25, Pd50PTFE50, and Pd25PTFE75 films were fabricated by simultaneously sputtering Pd and PTFE at the indicated power and for the indicated time. Subsequently, an annealing procedure was followed (see the text). The thickness referred to in the table is the intended nominal thickness before annealing. The thickness was scaled in such a way that the number of Pd atoms in each sample is approximately the same. The tilt of the Pd gun is defined as the angle away from the direct line of sight between the sputter target and the substrate.

made roughly a factor of 3 thinner (33 nm) than for the other measurements to enhance the sensitivity of the technique.

2.2. Structural Measurements. Grazing-incidence X-ray diffraction (GIXRD) and X-ray reflectometry (XRR) measurements were performed with a Bruker D8 Discover (Bruker AXS GmbH, Karlsruhe, Germany). This diffractometer is equipped with a LYNXEYE XE detector operating in 0D high count-rate mode and a Cu−Kα, λ = 0.1542 nm X-ray source. For the GIXRD measurements, an incident angle of ω = 0.6° was used, and a Göbel mirror in combination with an exit slit of 0.2 mm was used on the primary side. On the secondary side, a 2.5° Soller slit was used. The GIXRD data were corrected for the background by subtracting the signal of an empty substrate measured under identical conditions.

For the XRR measurements, a Göbel mirror in combination with an exit slit of 0.1 mm on the primary side were used. On the secondary side, two 0.1 mm slits were used to control the divergence of the beam. The XRR data are fitted with GenX3[37,38] to obtain estimates of the layer thickness, scattering length density, and roughness of the film.

Neutron reflectometry measurements were performed at the time-of-flight neutron reflectometer ROG connected to the 2.3 MW HOR reactor of the Delft University of Technology, Delft, The Netherlands.[39] During the time of the measurements, the reflectometer was connected to a thermal neutron source. The settings chosen were a chopper frequency of 17.7 Hz with an interdisc distance of 0.280 m, an incident angle of 8.5 mrad, and a first and second slit width of 1.5 and 0.75 mm, respectively. Together, these settings resulted in a footprint of $65/80 \times 40$ mm² (umbra/penumbra) and a resolution of $\Delta Q/Q \approx 5\%$. To expose the cell to different partial hydrogen pressures at $T = 22$ °C, the sample was positioned inside the temperature- and pressure-controlled cell described in ref 40. Subsequently, the absolute pressure of the gas mixtures of 4.00 ± 0.08% H_2 and 96.00% Ar was varied between 10 mbar and 6.1 bar (Linde Gas Benelux BV, Dieren, The Netherlands). After setting the pressure, we waited at least 10 min to commence the measurement to ensure that the sample was in equilibrium with its environment. A model was fitted to the data using GenX3[37,38] to obtain quantitative estimates of the thickness, scattering length density, and roughness of the sample. The hydrogen-to-metal ratio was calculated using the procedure outlined in the Supporting Information of ref 41. In the analysis, we made the assumption that the PTFE composition is unaffected by the hydrogen absorption. We note that as the Pd only constitutes 25% of the total material, the error bar of the hydrogen-to-metal ratio is larger than in other neutron reflectometry experiments.

X-ray photoelectron spectroscopy (XPS) measurements were performed with a ThermoFisher K-Alpha spectrometer with a monochromatic Al Kα (1486.6 eV) X-ray source operating at 36 W (12 kV, 3 mA), a flood gun operating at 1 V, 100 μA, a pass energy of 50 eV and a spot size of approximately 800×400 μm² (Thermo Fisher Scientific Inc., Waltham, MA, United States of America). The base

pressure in the analysis chamber was approximately 2×10^{-9} mbar. The binding energy was corrected for the charge shift using the primary C 1s hydrocarbon peak at BE = 284.8 eV as a reference, while the spectrometer was calibrated using an Au reference sample. The ThermoFisher Avantage software was used to fit the data using the weighted least-squares fitting method and a nonlinear Shirley-type background, a pseudo-Voight peak shape with a fixed Lorentzian−Gaussian ratio.

Scanning transmission electron microscopy (STEM) and STEM energy dispersive X-ray (EDX) analyses were performed using a ThermoFisher Spectra Ultra microscope equipped with a field emission gun (X-FEG) with double correctors for probe and image formation. It is equipped with an UltiMono electron source. The microscope was operated at 300 kV to record high-angle annular dark field (HAADF) images with a probe convergence angle of 21.4 mrad with a 50 μm condenser aperture. STEM EDX was performed using ultra-X, which provides a solid angle of >4.4 Sr. The STEM EDX was performed using an 8.5 mrad convergence angle with a 20 μm condenser aperture.

2.3. Optical Measurements. Optical transmission measurements as a function of partial hydrogen pressure were performed with the hydrogenography setup at multiple temperatures.[42] This setup consists of a pressure cell located inside an oven (Genlab, Widnes, United Kingdom). Windows on the top and bottom of the pressure cell allow light to be transmitted from the five Philips MR16 MASTER LEDs (10/50 W) with a color temperature of 4000 K light source through the samples to the Imaging Source DFK 23UM021 1/3 in Aptina CMOS MT9M021 1280 × 960 pixels color camera with an Edmunds Optics 55-906 lens. This camera records the red, green, and blue transmissions separately. The transmission is averaged over an area of approximately 80 mm² corresponding to roughly 100 × 100 pixels. An Al reference sample is used to compensate for fluctuations of the LED white light source.

To vary the partial hydrogen pressures between $10^{-1} < P_{H_2} < 10^6$ Pa, we change the absolute pressure inside the pressure cell by changing the absolute hydrogen pressure of 0.10, 4.0, and 100% H_2 in Ar gas mixtures ($\Delta c_{H_2}/c_{H_2} < 2\%$, Linde Gas Benelux BV, Dieren, The Netherlands). Typical gas flows are 20 s.c.c.m. for increasing pressure steps and 100 s.c.c.m. for decreasing pressure steps. A more detailed description of the optical measurements can be found in ref 43.

The absolute transmission measurements were performed using an Ocean Optics HL-2000-FSHA halogen light source and an Ocean Optics Maya2000 Pro Series Spectrometer (Ocean Insights Orlando, FL, United States of America). The intensity measured by the spectrometer is corrected for the background by subtracting a spectrum measured with a closed shutter from the measured intensity.

3. RESULTS

3.1. Fabrication and Structure of the Samples. The fabrication of the thin films consists of two steps: (i) a codeposition step and (ii) a thermal annealing step. It starts by cosputtering Pd (direct current magnetron sputtering) and PTFE (radiofrequency magnetron sputtering) in different ratios on quartz substrates or TEM grids (see experimental methods for more details). We have selected four ratios: 25% Pd and 75% PTFE (Pd25PTFE75), 50% Pd and 50% PTFE (Pd50PTFE50), 75% Pd and 25% PTFE (Pd75PTFE25), and a sample with 100% Pd and a 30 nm PTFE layer on top (Pd+PTFE). Here, the ratios refer to the volumetric ratios determined from individually sputtering the two targets (see the experimental methods). To ensure that the number of Pd atoms in each sample is approximately the same, we scaled the thickness with the inverse of the Pd concentration. This yielded a nominal thickness varying from 30 nm for the 100% Pd sample to 120 nm total thickness of the Pd25PTFE75 sample (Table 1).

Figures 1 and 2a,b show photographs of the films produced by codepositing. Remarkable is that despite that the number of Pd atoms is roughly the same in each of the as-prepared films and
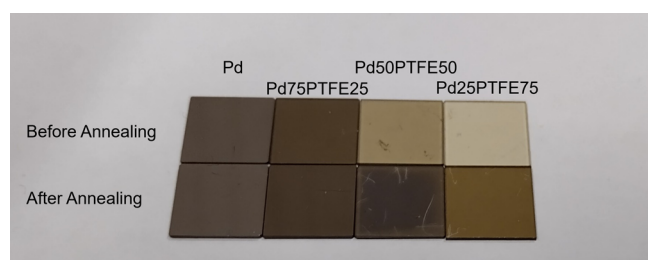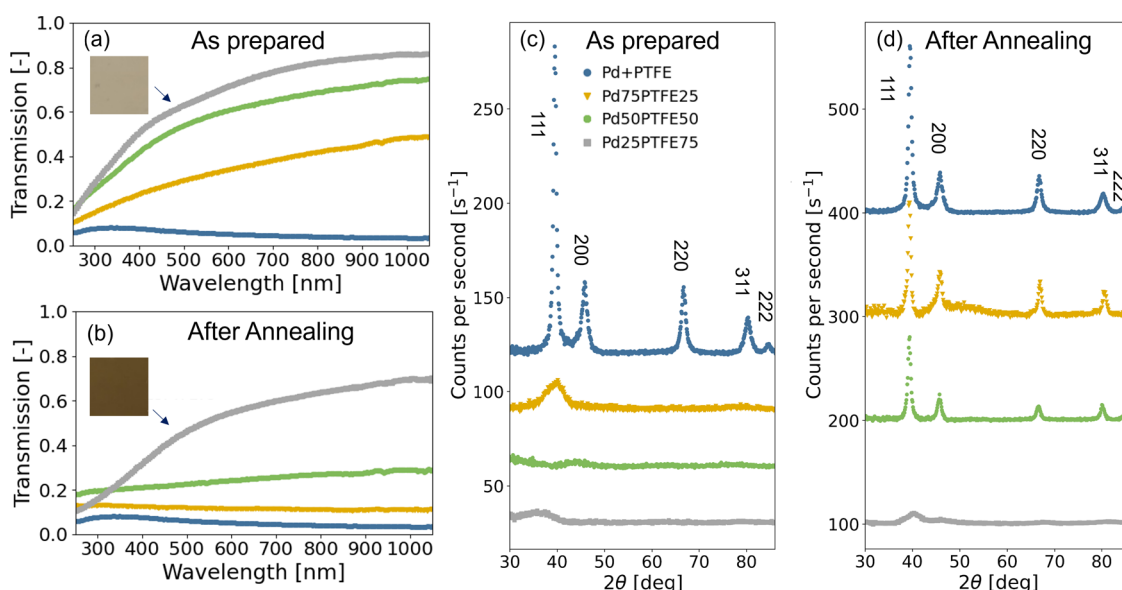
Figure 1. Photographs of the samples before and after annealing for 4 days at 200 °C during which the samples were exposed to 8 cycles of hydrogen. The Pd + PTFE sample consists of a Pd layer, followed by a PTFE layer. The Pd75PTFE25, Pd50PTFE50, and Pd25PTFE75 samples are produced by cosputtering Pd and PTFE in different volumetric ratios followed by an annealing step (see experimental details).

the pure Pd is clearly metallic (Figure 1), the composite films have a more insulating nature and become almost fully transparent with a brown-yellowish color for Pd25PTFE75 (Figure 2a). As we will see below, the transparent nature of the films is due to the agglomeration of the Pd atoms in nanoparticles, while the brownish color is attributed to (localized) surface plasmon resonances (LSPR): when a metal-dielectric interface or a metal nanoparticle is exposed to light, the oscillating field of the light causes electrons in the metal (particle) to oscillate coherently. This, in turn, causes an absorption maximum at a particular wavelength that depends on the shape, size, and type of metal and dielectric medium.[34] As the metallic particles in the sample are likely polydisperse, the LSPR absorption wavelength varies widely across the sample, causing a brownish color of the sample. This is consistent with the optical transmission measurements of Figure 2a,b, which show a wide range of wavelengths at which the optical transmission is decreased rather than a sharp dip.

The second step in fabricating the samples is thermal annealing under hydrogen. The idea behind this step is to ensure agglomeration of the Pd atoms within the thin film, such that they form small nanoparticles inside a polymer matrix. To do this, we exposed the samples for 4 days to 200 °C and 8 cycles of hydrogen. The annealing temperature was chosen to be high enough to allow palladium atom reorganization, yet low enough not to melt the polymer. The exposure to 8 cycles of hydrogen between 0 and 10 bar results in additional settling of the microstructure such that the material becomes structurally stable.

The annealing has a profound influence on the optical properties of the samples. The samples become notably darker (Figure 1), and with the exception of the Pd25PTFE75 sample, have a more metallic character. This is confirmed by the optical transmission measurements, which show for the Pd75PTFE25 and Pd50PTFE50 a more comparable transmission to that of Pd than to that of Pd25PTFE75. The fact that the character of the Pd75PTFE25 and Pd50PTFE50 became more metallic suggests that, in these cases, no individual nanoparticles in a polymer matrix are formed. Therefore, the Pd25PTFE75 sample is the most likely candidate for this.

XRR, a technique in which the reflectivity of X-rays of a material is measured as a function of glancing angle to obtain information about the thickness, roughness, and density of thin films, shows that annealing induces a densification of the material (Figure 3). The shift of the critical edge, that is, the angle at which the reflected X-ray intensity drops significantly, shifts for each sample to higher angles after annealing. Careful fitting of the XRR data to a one-layer model resulted in scattering length density (SLD) profiles. The SLD can, in the case of X-ray, be interpreted as a quantity that is roughly proportional to the electron density of the material. These SLD profiles confirm the densification of the film after annealing and indicate a concurrent decrease in layer thickness.

Figure 2. Optical transmission and grazing incidence X-ray diffraction (GIXRD) data of the (a, c) as-prepared samples and the (b, d) samples after annealing for 4 days at 200 °C during which the samples were exposed to 8 cycles of increasing and deceasing pressures of hydrogen. The Pd + PTFE sample consists of a Pd layer followed by a PTFE layer. (a, b) Wavelength dependence of the optical transmission. (c, d) GIXRD diffraction patterns. The data are vertically shifted to facilitate an improved presentation. The inset in (a, b) show color photographs of the Pd25PTFE75 sample before and after annealing.
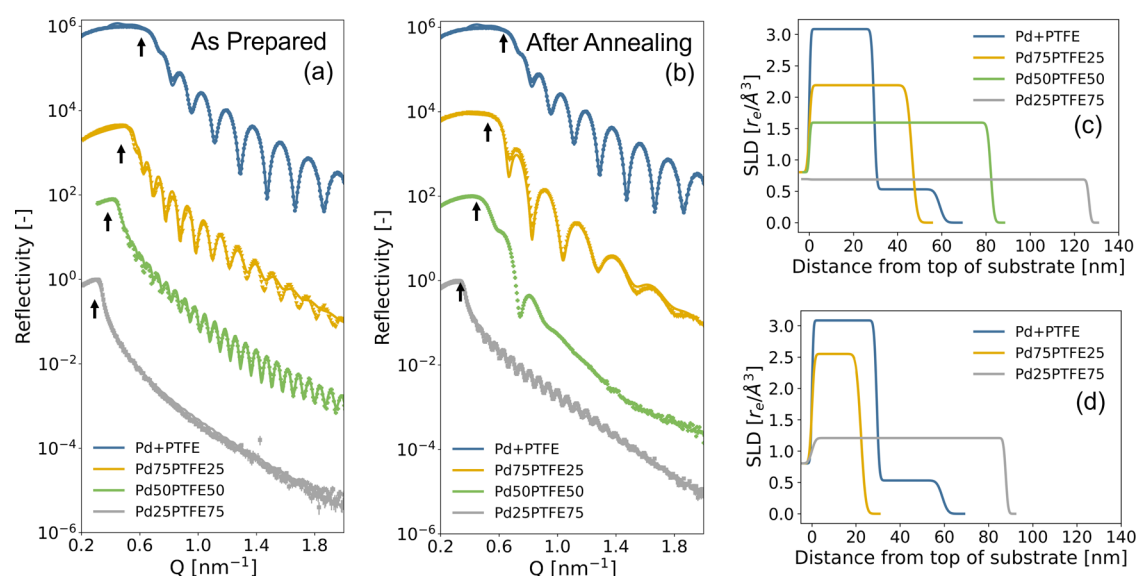
Figure 3. X-ray reflectometry (XRR) data of the (a, c) as prepared samples and the (b, d) samples after annealing for 4 days at 200 °C during which the samples were exposed to 8 cycles of increasing and deceasing pressures of hydrogen. (a, b) Measured XRR data and the corresponding fits to the data (continuous lines). The critical angle, indicated by an arrow, shifts to higher angles with increasing electron density of the film. (c, d) Scattering length density (SLD) plots, obtained by fitting the data to a one-layer model. For the Pd50PTFE50 sample after annealing no satisfactory fit could be obtained. The data are vertically shifted to facilitate an improved presentation.
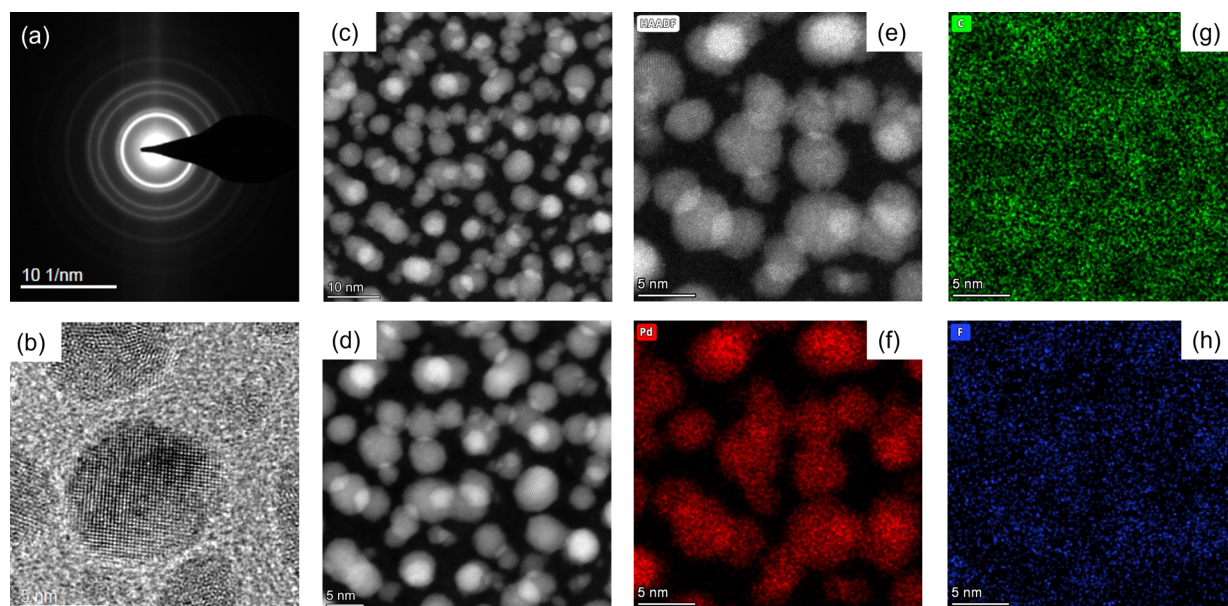

Figure 4. Transmission electron microscopy (TEM) measurements of the Pd25PTFE75 sample after annealing for 4 days at 200 °C during which the samples were exposed to 8 cycles of increasing and deceasing pressures of hydrogen. (a) Electron diffraction pattern, where the rings correspond to the (111), (200), (220), (311), and (222) lattice planes as seen from the inner to the outer ring. (b) High-resolution TEM image showing (200) lattice planes. (c–e) Scanning transmission electron microscopy (STEM) images at various magnification levels. (f–h) (S)TEM energy-dispersive X-ray (EDX) spectroscopy elemental compositional maps of (f) palladium, (g) carbon, and (h) fluorine.

Moreover, GIXRD shows that the annealing induces in the Pd25PTFE75 film the formation of Pd nanoparticles in presumably a PTFE matrix. Differently, for the other composite films, the diffraction patterns resemble those of a pure Pd film. Grazing-incidence diffraction, in which the sample was exposed to X-rays under a constant angle of $\omega = 0.6°$ while the detector angle was varied to scan 2θ, was chosen as it yields a much higher sensitivity than commonly used Bragg–Brentano diffraction in the case of thin films. In the latter technique, both the incident and detector angles are moved synchronously and this way

resulting in barely any signal when the film is thin (Figure S2). While before annealing no peak appears in the diffraction pattern of Pd25PTFE75 around $2\theta = 40°$ (Figure 2c), i.e., the expected position for the Pd⟨111⟩ face-centered cubic (fcc) peak, a clear peak with a maximum at $2\theta = 40.17°$ is observed after annealing (Figure 2d). The position corresponds to a lattice constant of $a = 0.389 \pm 0.002$ nm, which is similar to that of bulk Pd ($a = 0.389 \pm 0.0001$, e.g., powder diffraction files (PDF) 05-0681, 46-1043, or 65-6174). The width of this peak is large, and as the width of the peak is inversely proportional to the
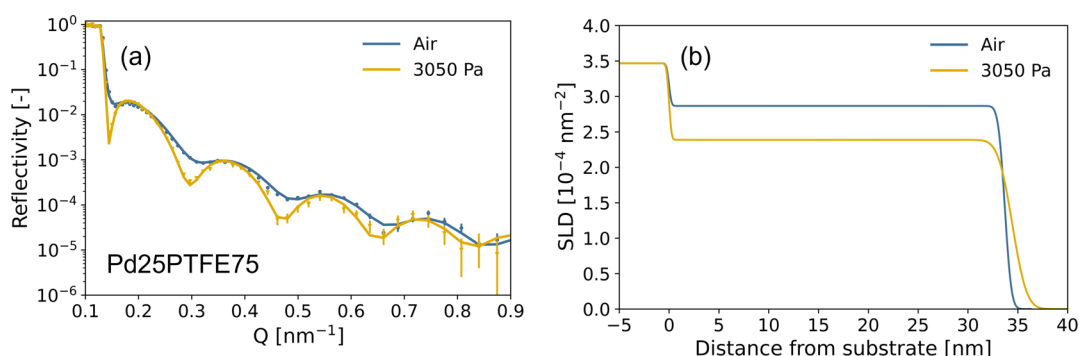
Figure 5. In situ neutron reflectometry results of a 34 nm Pd25PTFE75 thin film after annealing as measured in air and at a partial hydrogen pressure of $P_{H_2} = 3048$ Pa at room temperature. (a) Neutron reflectometry data as a function of the momentum transfer Q. The points indicate the measured data, and the continuous lines are fits to it. (b) Corresponding scattering length density profile. The film hydrogenates at $P_{H_2} = 8600$ Pa to approximately PdH$_{0.7}$ with a total expansion of the film of approximately 2%.
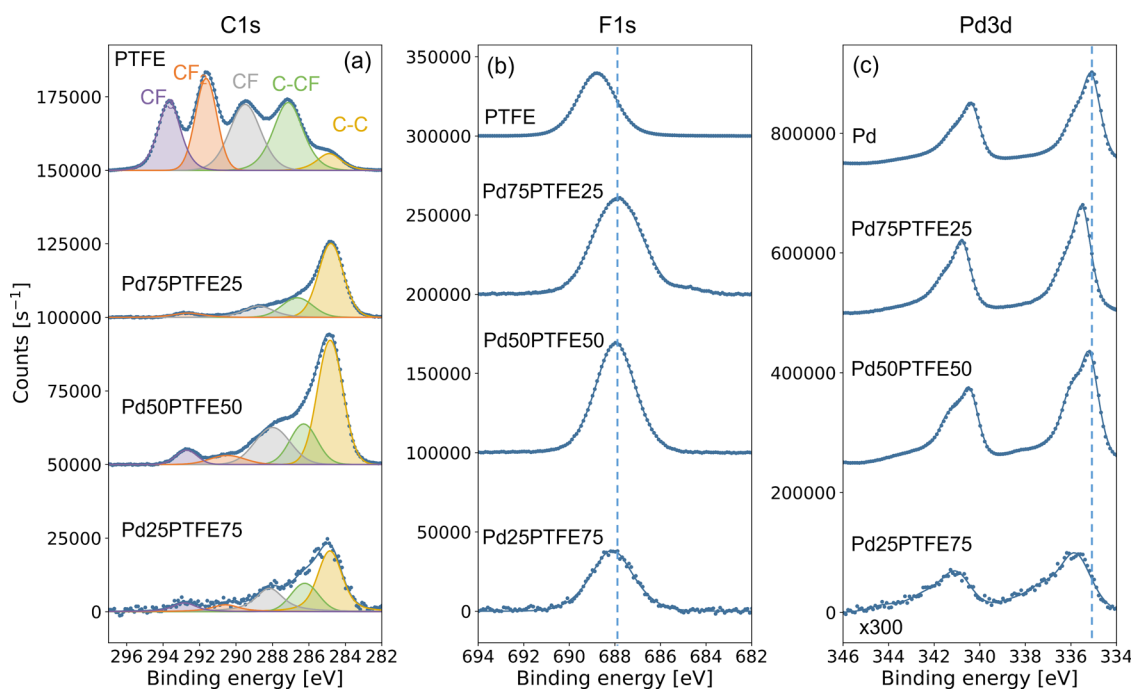
Figure 6. X-ray photoelectron spectroscopy (XPS) results of the Pd75PTFE25, Pd50PTFE50, and Pd25PTFE75 samples, as well as a sputtered PTFE or Pd reference sample. The Pd75PTFE25, Pd50PTFE50, and Pd25PTFE75 samples are produced by cosputtering Pd and PTFE in the different volumetric ratios followed by an annealing step (see experimental details). Panel (a) shows the detailed scan around the C 1s binding energy that is fitted to 5 pseudovoigt functions and a nonlinear Shirley-type background. These pseudovoigt peaks represent the different chemical bonds indicated in the figure. Panel (b) shows the detailed scans around the F 1s binding energy and (c) around the Pd 3d binding energy. The vertical dashed lines serve as a guide to the eye. The data are vertically shifted to facilitate an improved presentation. The Pd 3d signal of the Pd25PTFE75 sample has been multiplied by a factor 300 to improve the presentation.

size of a crystallite, it is consistent with the formation of very small crystallites with an fcc lattice. Differently, the X-ray diffraction patterns for Pd75PTFE25 and Pd50PTFE50 show relatively sharp diffraction peaks as those for Pd (Figure 2d), indicative of much larger crystallites.

To obtain a quantitative estimate of the characteristic size of the nanoparticles, we employ Scherrer's equation that relates the width of a diffraction peak to the typical size of the crystallites in a material: $D = K\lambda/\beta \cos\theta$, where λ is the X-ray's wavelength, β the fwhm of the peak in degrees, and K a shape factor that is 0.9 for spherical particles.[44] Performing the analysis on the annealed samples provides a characteristic crystallite size of about 5 nm for Pd25PTFE75, while for the other samples, including Pd, a crystallite size of about 20 nm is obtained. We wish to note that

this is a very crude approximation as the particles do not necessarily need to be spherical and as it ignores other contributions to peak broadening, such as microstrain.

TEM confirms that annealing induces the formation of crystalline Pd nanoparticles in a polymer matrix. To allow transmission of an electron beam, Pd75PTFE25 samples were also prepared and annealed on SiN TEM grids under exactly the same conditions as the samples on quartz substrates. This is also highlighted by the electron diffraction patterns (Figures 4a and S3b,d), showing a stark contrast before and after annealing: before annealing, no sharp diffraction rings are visible, while after annealing, sharp rings emerge, indicating the presence of crystalline Pd. The TEM images of Figure 4b confirm this and

display nanoparticles around 5 nm in size, which is in excellent agreement with the GIXRD data.

Most importantly, STEM shows that the majority of the nanoparticles are free-standing and not clamped to the substrate. Indeed, the STEM images portrayed in Figure 4c–e show that the nanoparticles are 'floating' in the polymer matrix and are present at various depths inside the film. Comparing the complementary EDX spectroscopy composition maps of Figure 4f–h with the corresponding STEM image provides further support for the formation of Pd nanoparticles and the fact that no significant quantities of individual Pd atoms are found inside the polymer matrix. As such, we established a method that can successfully produce Pd particles in a polymer matrix. In addition, based on the obtained SLD derived from XRR of the film (1.2×10^{-2} nm^{-2}), and comparing it with that of Pd (3.1×10^{-2} nm^{-2}) and sputtered PTFE (0.6×10^{-2} nm^{-2}) for the case of the Pd25PTFE75 film, we deduce that the volume fraction of the Pd nanoparticles is approximately 25%, consistent with what is expected based on the sputtered ratios.

We employ in situ neutron reflectometry to obtain quantitative data of the expansion of the film and the hydrogen-to-metal ratio of the palladium nanoparticle when it is exposed to a partial hydrogen pressure of P_{H_2} = 8600 Pa. Analogue to X-ray reflectometry, in neutron reflectometry the reflectivity of neutrons by a material is measured as a function of glancing angle to obtain information about the thickness, roughness, and composition of thin films. The major difference with X-ray reflectometry is that neutrons interact with the core of an atom rather whereas X-rays interact with the electrons in the material. As the interaction with the core of the hydrogen atom is relatively strong, this allows for the quantification of the hydrogen-to-metal ratio. The resulting measurements, provided in Figure 5, show a total volume expansion of about 2% at the highest partial hydrogen pressure measured. At this pressure, the Pd nanoparticles are hydrogenated to $PdH_{0.7}$, which is similar to bulk.[8,9] We note that as the volume fraction of the Pd nanoparticles is around 25%, this implies a volumetric expansion of around 8% of the Pd crystallites, which also corresponds well with the values reported for bulk Pd.[8,9]

XPS is used to establish whether the properties of the polymer are altered by the annealing of the samples. This plays an important role in hydrogen sensing applications, as PTFE can accelerate the hydrogenation kinetics of palladium substantially by at least a factor of 5. Two mechanisms have been proposed to explain this acceleration. First of all, it can keep the palladium surface clean such that all Pd sites remain available for catalyzing the hydrogen dissociation reaction and the absorption of hydrogen by the lattice.[27] Second, it has been shown that the presence of PTFE shifts the binding energy of the Pd 3d electrons, which is linked to a lower activation energy of the hydrogen dissociation reaction, resulting in accelerated kinetics.[25,28] As such, from a (hydrogen sensing) application perspective, it is desirable that the structural integrity and thus the chemical bonds within the coating stay intact. It is important to note here that the structure of sputtered PTFE is substantially different from that of bulk PTFE: rather than predominantly consisting of C–F_2 bonds, sputtered PTFE also features CF, CF_3, C–C, and C–CF bonds, typically in approximately equal ratios.[27,29,45−47]

The results, depicted in Figure 6a, show that compared to the reference sputtered PTFE sample, the ratio of bonds has been altered substantially after annealing. We find that most C atoms

bond to another C atom, and that the amount of carbon–fluorine bonds has decreased substantially. Nevertheless, a substantial fraction of C–F bonds is still present in the samples. These results are consistent with the F 1s scans depicted in Figure 6b in which a shift of the binding energy of fluorine is seen. Most importantly, we observe a small shift in the binding energy by about 0.5 eV of the Pd 3d electrons between the metallic Pd film and the Pd-PTFE composite films, even after annealing. This has previously[28,29] been linked to a reduced activation energy of the hydrogen dissociation reaction and fast hydrogenation kinetics. In the next section, we will study how the films respond to hydrogen and the hydrogenation kinetics.

3.2. Application as a Hydrogen Sensing Material. As the next step, we consider how the sample responds to hydrogen. This is, for example, important for hydrogen sensing applications, where a gradual change of the metal-to-hydrogen ratio of the material is required to enable a smooth change of the optical properties over a large partial hydrogen pressure/concentration window.

To study the hydrogenation of the Pd nanoparticles embedded in the PTFE matrix, we use optical transmission measurement (hydrogenography).[48] We expose the particles first to a stepwise increase in partial hydrogen concentration and subsequently to a stepwise decrease. Simultaneously, we record the optical transmission, which we normalize to the optical transmission of the film in the absence of hydrogen to obtain the relative optical transmission. Both the logarithm of the relative changes of the transmission ($Ln(\mathcal{T}/\mathcal{T}_{prep})$) and the partial hydrogen pressure is plotted as a function of time in Figure 7.
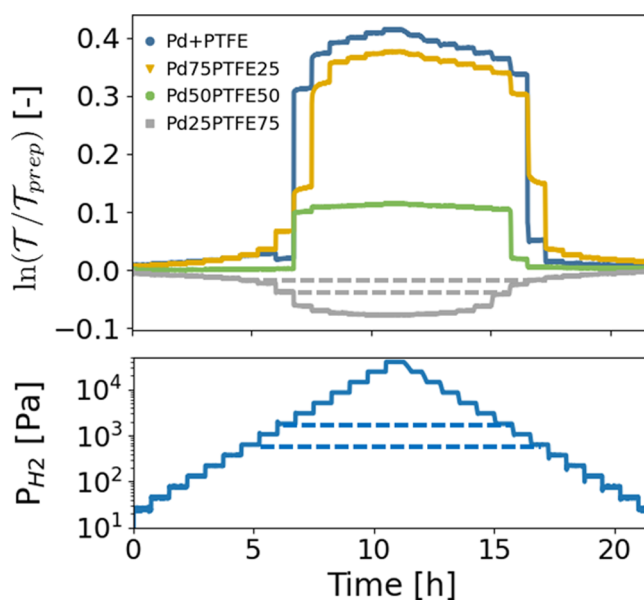
Figure 7. Changes of the green light optical transmission $\mathcal{T}$ of the Pd+PTFE, Pd75PTFE25, Pd50PTFE50, and Pd25PTFE75 samples after annealing. The Pd+PTFE sample consists of a Pd layer followed by a PTFE layer. The Pd75PTFE25, Pd50PTFE50, and Pd25PTFE75 samples are produced by cosputtering Pd and PTFE in the different volumetric ratios followed by an annealing step (see experimental details). The optical transmission is measured as a function of time and relative to the transmission of the film after annealing ($\mathcal{T}_{prep}$). The film was exposed at T = 28 °C to various increasing and decreasing pressure steps, during which the optical transmission was recorded. The horizontal dashed lines serve as a guide to the eye and indicate levels of the same partial hydrogen pressure and optical transmission.
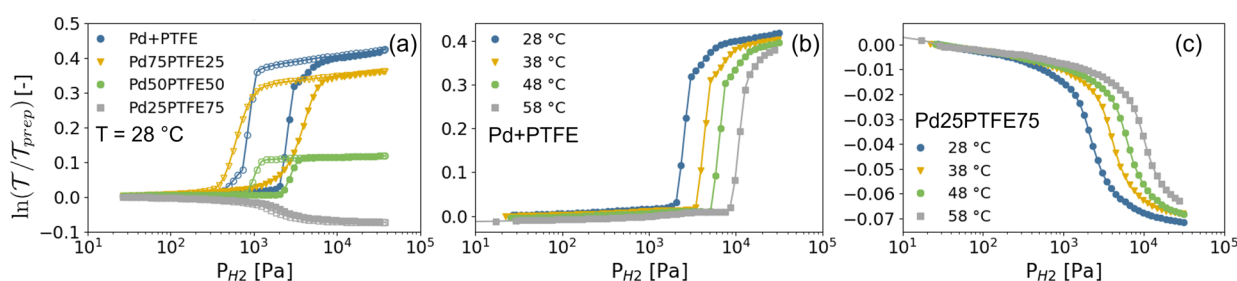
Figure 8. Partial hydrogen pressure and temperature dependence of the optical transmission of green light $\mathcal{T}$ of the Pd + PTFE, Pd75PTFE25, Pd50PTFE50, and Pd25PTFE75 samples after annealing. The Pd + PTFE sample consists of a Pd layer followed by a PTFE layer. The Pd75PTFE25, Pd50PTFE50, and Pd25PTFE75 samples are produced by cosputtering Pd and PTFE in the different volumetric ratios followed by an annealing step (see experimental details). The optical transmission is measured relative to the optical transmission of the as-prepared state ($\mathcal{T}_{prep}$). Each data point corresponds to the optical transmission after exposing the film for at least 30 min to a constant pressure. The closed data points correspond to increasing pressure steps and the open ones to decreasing pressure steps. Panel (a) presents the pressure dependence for the different samples. Panel (b, c) present the pressure dependence of the changes in optical transmission for (b) the Pd and (c) Pd25PTFE75 films at different temperatures.

This figure reveals that for each step in partial hydrogen pressure, there is a well-defined optical transmission level that is stable across time. For all cases, substantial optical changes are observed before and around P_{H_2} = 4000 Pa (c_{H_2} = 4%), i.e., the explosive limit in air, which is beneficial for hydrogen sensing applications.

The data in Figure 7 can be summarized by taking the average optical transmission of each step in pressure, after both increasing and decreasing pressure steps. In this way, the pressure-transmission-isotherms (PTIs) are obtained, which show the optical transmission as a function of the partial hydrogen pressure at a constant temperature. Comparing the PTIs of the different samples in Figures 8 and S4 reveals three remarkable observations. First of all, while for Pd thin films we observe an increase in the optical transmission when the film is exposed to hydrogen, for the nanoparticles in the Pd25PTFE75 film, we observe the reverse. We attribute the opposite optical response to different dominating effects. For pure Pd, the increase of the optical transmission is attributed to changes in the band structure of the material when hydrogen is absorbed by the material (see, e.g., refs 49−51). This causes palladium to become more transparent. Differently, for the nanoparticles, the optical transmissions could be approximated as a weighted sum of areas with a relatively high transmission, i.e., PTFE, where no nanoparticle is present, and areas with a fairly low transmission, i.e., the Pd nanoparticles. Upon hydrogen absorption by the palladium nanoparticle, the particle expands. As such, the relative weight of the low transmission Pd nanoparticle with increasing partial hydrogen pressure increases, causing an overall decrease in the optical transmission. As a very simplistic model, we can consider the Beer−Lambert Law. When the nanoparticles are exposed to hydrogen, they expand by about 8% in volume (see the neutron reflectometry results). Consequently, this would, according to the Beer−Lambert Law, result in a decrease of the optical transmission by 8%, which corresponds well with the observed decrease in optical transmission of about 7%. We note that apart from absorption effects, light scattering and other effects may play an important role in explaining the (change in) optical transmission when the particles are exposed to a hydrogen-containing atmosphere.

Second, we find that the Pd nanoparticles hydrogenate much more gradually than the Pd thin film. This is consistent with reports in the literature and beneficial for hydrogen sensing applications. Indeed, Figure 8 shows that the Pd thin film shows a step-like change in the optical transmission with increasing

partial hydrogen pressure,[52,53] while a more gradual evolution of the optical transmission is seen with increasing partial pressure for the Pd25PTFE75 film. There could be at least two explanations for this: The TEM images in Figure 4 show that the shape of the nanoparticles does not seem to be spherical but appears more faceted. In many cases, it most closely seems to resembles an icosahedron shape. This would be in line with previous research that reported such a shape for small Pd particles (e.g., 7 nm[7]). For this case, a single-phase particle has also been reported in which any hydrogen-to-metal ratio can occur depending on hydrogen pressure. In other words, the pressure-transmission/composition-isotherm would vary gradually with the partial hydrogen pressure.[7] Furthermore, the sample is not composed of a single-sized nanoparticle but rather a distribution of sizes and possibly also shapes. As the plateau pressure of small nanoparticles is found to be size dependent, at a given pressure around the absorption plateau pressure, only a fraction of the particles will be transformed into the β-phase (see, e.g., refs 1−7). The optical transmission measurements reflect the properties of an ensemble of nanoparticles, and as such, the PTIs are naturally smeared out over a larger pressure region and become more gradual in nature. As a side note, the Van't Hoff analysis presented in Figure S5 shows that the enthalpy and entropy of hydrogenation at the plateau are approximately the same for all samples: -42 ± 2 and 104 ± 5 kJ $mol_{H_2}^{-1}$, respectively, which is consistent with the values reported in ref 3.

Third, we also observe that at room temperature the optical transmission of the Pd25PTFE75 film already starts to change for $P_{H_2} \gtrsim 20$ Pa (corresponding to a hydrogen concentration of 0.02% in Ar), a pressure lower than that for the Pd thin film that shows only a minor optical change before the onset of the plateau at $P_{H_2} \gtrsim 2000$ Pa. It is consistent with previous research that the solubility window of hydrogen in small Pd nanoparticles is substantially enlarged. This finding is beneficial for optical hydrogen sensing applications, as it allows hydrogen to be detected optically at lower partial hydrogen pressures and over a much larger pressure window. Nevertheless, even for the Pd25PTFE75, a relatively modest hysteresis remains present, although substantially smaller than for the Pd film. The larger sensing range and reduced hysteresis thus make the nanocomposite film an improved material with respect to Pd films.

Fast kinetics is also an important aspect for hydrogen sensor applications. To study this, we report in Figure 9 the response
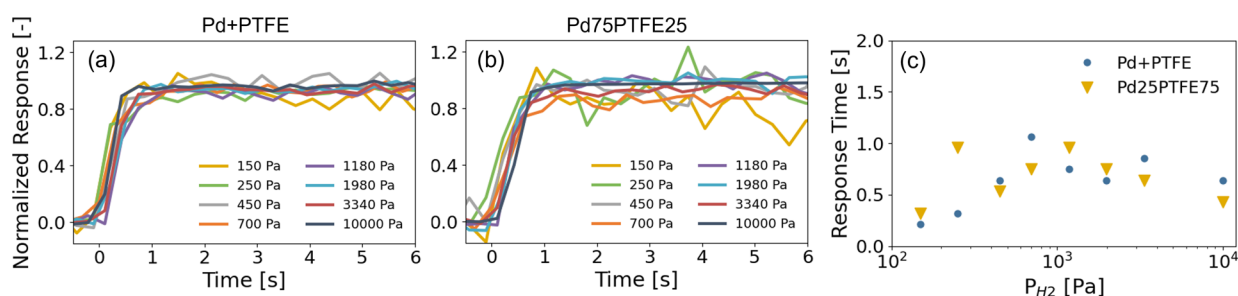
Figure 9. Adsorption kinetics of the Pd+PTFE and Pd25PTFE75 samples after annealing at T = 48 °C. Panels a and b show the normalized responses of the samples to a series of pressure steps between P_{H_2} = 0.5×10^2 Pa and the partial hydrogen pressure indicated for the Pd + PTFE and Pd25PTFE75, respectively. (c) Partial hydrogen pressure dependence of the response time of the thin films. The response time is defined as the time to reach 90% of the total signal.

time to an increasing step in hydrogen pressure. These response times correspond to the time at which 90% of the final optical response is observed. The response times are, for all partial hydrogen pressures considered, less than or around 1 s. As this corresponds to approximately the intrinsic response time of the experimental setup, it could well be that the response times are even faster. Indeed, although the response time of the material is expected to drop with increasing partial hydrogen pressure, we do not observe such a trend. This hints that at higher pressures, where it takes longer for the setup to reach the desired partial hydrogen pressure, the measurements reflect the intrinsic response time of the setup. Most importantly, the measurements illustrate that the goal of achieving a fast response material has been realized. Furthermore, for the Pd+PTFE reference sample, we observe a relatively noisy signal at lower hydrogen pressures. This stems from the small optical contrast observed in this pressure regime for Pd, while the Pd25PTFE75 sample has a larger optical response (and thus larger sensitivity as a hydrogen sensing material) due to the more gradual hydrogenation of the sample at lower hydrogen pressures (see Figure 8). This highlights the advantage of using nanoparticles instead of a continuous Pd film.

4. CONCLUSIONS

In conclusion, we have successfully synthesized palladium nanoparticles that are embedded in a polymer matrix using magnetron cosputtering and a subsequent thermal annealing step. These palladium nanoparticles have a characteristic size of approximately 5 nm, as identified with TEM and GIXRD measurements. Furthermore, the effect of hydrogen on the optical transmission of the nanoparticles is opposite that of continuous thin films: Whereas for thin films the material becomes more transparent upon hydrogen absorption as a result of the change of the dielectric function, for nanoparticles the changes in optical transmission make the sample more opaque and can be explained by considering the expansion of the particle upon absorption. The gradual change of the optical transmission of the nanocomposite film across a wide range of partial hydrogen pressures with subsecond response time makes the material suitable for optical hydrogen sensing, despite a relatively small hysteresis. In a more general perspective, we have thus illustrated that cosputtering of a polymer and a metal, followed by annealing, is a scalable method to produce nanoparticles embedded in a polymer matrix. In further research, the annealing temperature and polymer-to-metal sputtering ratio can be tuned to control the size and density of metallic particles inside the polymer matrix. In addition, other materials, including metallic alloys, can be considered, such as palladium–gold alloys for hydrogen sensing applications.

ASSOCIATED CONTENT

Supporting Information

The Supporting Information is available free of charge at https://pubs.acs.org/doi/10.1021/acsaem.4c03202.

> Schematic of the geometry of the magnetron sputtering system, additional TEM images, Bragg–Brentano XRD patterns, partial hydrogen pressure and temperature dependence of the optical transmission, and Van't Hoff analysis of the enthalpy and entropy of the hydrogenation around the plateau pressure (PDF)

AUTHOR INFORMATION

Corresponding Author

Lars Johannes Bannenberg − *Faculty of Applied Sciences, Delft University of Technology, 2629 JB Delft, Netherlands;* orcid.org/0000-0001-8150-3694; Email: l.j.bannenberg@tudelft.nl

Authors

Gopi Krishnan − *National Center for Nano Fabrication and Characterization (DTU Nanolab), Technical University of Denmark (DTU), 2800 Kgs. Lyngby, Denmark*

Bart Boshuizen − *Faculty of Applied Sciences, Delft University of Technology, 2629 JB Delft, Netherlands;* orcid.org/0000-0002-3413-8839

Herman Schreuders − *Faculty of Applied Sciences, Delft University of Technology, 2629 JB Delft, Netherlands*

Complete contact information is available at:
https://pubs.acs.org/10.1021/acsaem.4c03202

Notes

The authors declare no competing financial interest.

REFERENCES

(1) Yamauchi, M.; Ikeda, R.; Kitagawa, H.; Takata, M. Nanosize effects on hydrogen storage in palladium. *J. Phys. Chem. C* **2008**, *112*, 3294−3299.

(2) Baldi, A.; Narayan, T. C.; Koh, A. L.; Dionne, J. A. In situ detection of hydrogen-induced phase transitions in individual palladium nanocrystals. *Nat. Mater.* **2014**, *13*, 1143−1148.

(3) Griessen, R.; Strohfeldt, N.; Giessen, H. Thermodynamics of the Hybrid Interaction of Hydrogen with Palladium Nanoparticles. *Nat. Mater.* **2016**, *15*, 311−317.

(4) Narayan, T. C.; Baldi, A.; Koh, A. L.; Sinclair, R.; Dionne, J. A. Reconstructing solute-induced phase transformations within individual nanocrystals. *Nat. Mater.* **2016**, *15*, 768−774.

(5) Sytwu, K.; Hayee, F.; Narayan, T. C.; Koh, A. L.; Sinclair, R.; Dionne, J. A. Visualizing facet-dependent hydrogenation dynamics in individual palladium nanoparticles. *Nano Lett.* **2018**, *18*, 5357−5363.

(6) Suzana, A. F.; Wu, L.; Assefa, T. A.; Williams, B. P.; Harder, R.; Cha, W.; Kuo, C.-H.; Tsung, C.-K.; Robinson, I. K. Structure of a seeded palladium nanoparticle and its dynamics during the hydride phase transformation. *Commun. Chem.* **2021**, *4*, 64.

(7) Zhou, S.; Figueras-Valls, M.; Shi, Y.; Ding, Y.; Mavrikakis, M.; Xia, Y. Fast and Non-equilibrium Uptake of Hydrogen by Pd Icosahedral Nanocrystals. *Angew. Chem., Int. Ed.* **2023**, *62*, No. e202306906.

(8) Manchester, F. D.; San-Martin, A.; Pitre, J. The H-Pd (hydrogen-palladium) system. *J. Phase Equilib.* **1994**, *15*, 62−83.

(9) Lewis, F. A.; Kandasamy, K.; Tong, X. Q. Palladium-hydrogen system. *Solid State Phenom* **2000**, *73-75*, 268−301.

(10) Hughes, R. C.; Ricco, A. J.; Butler, M. A.; Martin, S. J. Chemical Microsensors. *Science* **1991**, *254*, 74−80.

(11) Butler, M. A. Fiber optic sensor for hydrogen concentrations near the explosive limit. *J. Electrochem. Soc.* **1991**, *138*, L46−L47.

(12) Silva, S. F.; Coelho, L.; Frazão, O.; Santos, J. L.; Malcata, F. X. A review of palladium-based fiber-optic sensors for molecular hydrogen detection. *IEEE Sensors Journal* **2012**, *12*, 93−102.

(13) Perrotton, C.; Westerwaal, R. J.; Javahiraly, N.; Slaman, M.; Schreuders, H.; Dam, B.; Meyrueis, P. A reliable, sensitive and fast optical fiber hydrogen sensor based on surface plasmon resonance. *Opt. Express* **2013**, *21*, 382−390.

(14) Wadell, C.; Syrenova, S.; Langhammer, C. Plasmonic Hydrogen Sensing with Nanostructured Metal Hydrides. *ACS Nano* **2014**, *8*, 11925−11940.

(15) Ndaya, C. C.; Javahiraly, N.; Brioude, A. Recent advances in palladium nanoparticles-based hydrogen sensors for leak detection. *Sensors* **2019**, *19*, No. 4478.

(16) Hübert, T.; Boon-Brett, L.; Black, G.; Banach, U. Hydrogen Sensors—a Review. *Sens. Actuators B: Chem.* **2011**, *157*, 329−352.

(17) Bannenberg, L. J.; Boelsma, C.; Asano, K.; Schreuders, H.; Dam, B. Metal Hydride Based Optical Hydrogen Sensors. *J. Phys. Soc. Jpn.* **2020**, *89*, No. 051003.

(18) Bannenberg, L. J.; Heere, M.; Benzidi, H.; Montero, J.; Dematteis, E. M.; Suwarno, S.; Jaroń, T.; Winny, M.; Orłowski, P. A.; Wegner, W.; Starobrat, A.; Fijałkowski, K. J.; Grochala, W.; Qian, Z.; Bonnet, J. P.; Nuta, I.; Lohstroh, W.; Zlotea, C.; Mounkachi, O.; Cuevas, F.; Chatillon, C.; Latroche, M.; Fichtner, M.; Baricco, M.; Hauback, B. C.; El Kharbachi, A. Metal (boro-) Hydrides for High Energy Density Storage and Relevant Emerging Technologies. *Int. J. Hydrogen Energy* **2020**, *45*, 33687−33730.

(19) Darmadi, I.; Nugroho, F. A. A.; Langhammer, C. High-Performance Nanostructured Palladium-Based Hydrogen Sensors—Current Limitations and Strategies for Their Mitigation. *ACS Sens.* **2020**, *5*, 3306−3327.

(20) Koo, W.-T.; Cho, H.-J.; Kim, D.-H.; Kim, Y. H.; Shin, H.; Penner, R. M.; Kim, I.-D. Chemiresistive Hydrogen Sensors: Fundamentals, Recent Advances, and Challenges. *ACS Nano* **2020**, *14*, 14284−14322.

(21) Chen, K.; Yuan, D.; Zhao, Y. Review of Optical Hydrogen Sensors Based on Metal Hydrides: Recent velopments and Challenges. *Opt. Laser Technol.* **2021**, *137*, No. 106808.

(22) Zhang, Y.; Peng, H.; Qian, X.; Zhang, Y.; An, G.; Zhao, Y. Recent advancements in optical fiber hydrogen sensors. *Sensors Actuat. B: Chem.* **2017**, *244*, 393−416.

(23) Wang, G.; Dai, J.; Yang, M. Fiber-optic hydrogen sensors: a review. *IEEE Sens. J.* **2021**, *21*, 12706−12718.

(24) Bannenberg, L. J.; Boelsma, C.; Schreuders, H.; Francke, S.; Steinke, N.-J.; Van Well, A. A.; Dam, B. Optical Hydrogen Sensing Beyond Palladium: Hafnium and Tantalum as Effective Sensing Materials. *Sens. Actuators B: Chem.* **2019**, *283*, 538−548.

(25) Bannenberg, L. J.; Schreuders, H.; Dam, B. Tantalum-Palladium: Hysteresis-Free Optical Hydrogen Sensor over 7 Orders of Magnitude in Pressure with Sub-Second Response. *Adv. Funct. Mater.* **2021**, *31*, No. 2010483.

(26) Bannenberg, L. J.; Schreuders, H.; van Beugen, N.; Kinane, C.; Hall, S.; Dam, B. Tuning the properties of thin film TaRu for hydrogen sensing applications. *ACS Appl. Mater. Interfaces* **2023**, *15*, 8033−8045.

(27) Ngene, P.; Westerwaal, R. J.; Sachdeva, S.; Haije, W.; de Smet, L. C. P. M.; Dam, B. Polymer-Induced Surface Modifications of Pd-based Thin Films Leading to Improved Kinetics in Hydrogen Sensing and Energy Storage Applications. *Angew. Chem. Int. Ed.* **2014**, *53*, 12081−12085.

(28) Nugroho, F. A. A.; Darmadi, I.; Cusinato, L.; Susarrey-Arce, A.; Schreuders, H.; Bannenberg, L. J.; da Silva, Bastos; Fanta, A.; Kadkhodazadeh, S.; Wagner, J. B.; Antosiewicz, T. J.; Hellman, A.; Zhdanov, V. P.; Dam, B.; Langhammer, C. Metal-Polymer Hybrid Nanomaterials for Plasmonic Ultrafast Hydrogen Detection. *Nat. Mater.* **2019**, *18*, 489−495.

(29) Bannenberg, L. J.; Boshuizen, B.; Ardy Nugroho, F. A.; Schreuders, H. Hydrogenation kinetics of metal hydride catalytic layers. *ACS Appl. Mater. Interfaces* **2021**, *13*, 52530−52541.

(30) Darmadi, I.; Stolass, A.; Oestergren, I.; Berke, B.; Nugroho, F. A. A.; Minelli, M.; Lerch, S.; Tanyeli, I.; Lund, A.; Andersson, O.; et al. Bulk-processed Pd nanocube−poly (methyl methacrylate) nanocomposites as plasmonic plastics for hydrogen sensing. *ACS Appl. Nano Mater.* **2020**, *3*, 8438−8445.

(31) Ostergren, I.; Pourrahimi, A. M.; Darmadi, I.; da Silva, R.; StolasÌ́Ą, A.; Lerch, S.; Berke, B.; Guizar-Sicairos, M.; Liebi, M.; Foli, G.; et al. Highly permeable fluorinated polymer nanocomposites for plasmonic hydrogen sensing. *ACS Appl. Mater. Interfaces* **2021**, *13*, 21724−21732.

(32) Jeon, K.-J.; Moon, H. R.; Ruminski, A. M.; Jiang, B.; Kisielowski, C.; Bardhan, R.; Urban, J. J. Air-stable magnesium nanocomposites provide rapid and high-capacity hydrogen storage without using heavy-metal catalysts. *Nat. Mater.* **2011**, *10*, 286−290.

(33) Liang, H.; Chen, D.; Chen, M.; Li, W.; Snyders, R. Study of the synthesis of PMMA-Mg nanocomposite for hydrogen storage application. *Int. J. Hydrogen Energy* **2020**, *45*, 4743−4753.

(34) Schürmann, U.; Takele, H.; Zaporojtchenko, V.; Faupel, F. Optical and electrical properties of polymer metal nanocomposites prepared by magnetron co-sputtering. *Thin Solid Films* **2006**, *515*, 801−804.

(35) Faupel, F.; Zaporojtchenko, V.; Strunskus, T.; Elbahri, M. Metal-polymer nanocomposites for functional applications. *Adv. Eng. Mater.* **2010**, *12*, 1177−1190.

(36) Cao, Y.; Nogawa, K.; Kobayashi, N.; Masumoto, H. Fabrication of transition metal (TM= Fe, Co) difluorides−carbon nanocomposite films by magnetron co-sputtered deposition of Fe/Co and Teflon targets. *Appl. Phys. Express* **2021**, *14*, No. 075502.

(37) Björck, M.; Andersson, G. GenX: an Extensible X-ray Reflectivity Refinement Program Utilizing Differential Evolution. *J. Appl. Crystallogr.* **2007**, *40*, 1174−1178.

(38) Glavic, A.; Björck, M. GenX 3: the latest generation of an established tool. *J. Appl. Crystallogr.* **2022**, *55*, 1063−1071.

(39) Bannenberg, L. J.; Bresser, R.; van der Ende, P.; van Exter, M.; van Goozen, W.; Naastepad, F.; Thijs, M. A.; Verleg, M. N.; de Vroege, K.; Waaijer, R.; van Well, A. A. The completely renewed and upgraded neutron reflectometer at the TU Delft Reactor Institute. *Rev. Sci. Instrum.* **2023**, *94*, 113901.

(40) Bannenberg, L. J.; Exeter, M.; Verleg, M.; Van der Wal, E.; Boshuizen, B.; Thijs, M.; Parnell, S. R.; Schreuders, H. Versatile pressure and temperature controlled cell for neutron reflectometry and small-angle neutron scattering. *J. Neutron Res.* **2023**, *26*, 1−13.

(41) Bannenberg, L. J.; Verhoeff, D. J.; Jonckers Newton, N.; Thijs, M.; Schreuders, H. Structural and Optical Properties of Thin Film β-Ta

upon Exposure to Hydrogen to Asses Its Applicability as Hydrogen Sensing Material. *ACS Appl. Nano Mater.* **2024**, *7*, 1757−1766.

(42) Gremaud, R.; Slaman, M.; Schreuders, H.; Dam, B.; Griessen, R. An optical method to determine the thermodynamics of hydrogen absorption and desorption in metals. *Appl. Phys. Lett.* **2007**, *91*, 231916.

(43) Dewi, H. S.; Dissanayake, K. P.; Schreuders, H.; Groves, R. M.; Bannenberg, L. J. Metal hydride hydrogen sensing materials from 28°C to 270°C. *Int. J. Hydrogen Energy* **2024**, *84*, 606−614.

(44) Scherrer, P. Bestimmung der Grosse und inneren Struktur von Kolloidteilchen mittels Rontgenstrahlen. *Nach Ges Wiss Gott.* **1918**, *1918*, 98−100.

(45) Stelmashuk, V.; Biederman, H.; Slavinska, D.; Zemek, J.; Trchova, M. Plasma polymer films rf sputtered from PTFE under various argon pressures. *Vacuum* **2005**, *77*, 131−137.

(46) Drábik, M.; Polonskyi, O.; Kylián, O.; Čechvala, J.; Artemenko, A.; Gordeev, I.; Choukourov, A.; Slavínská, D.; Matolínová, I.; Biederman, H. Super-Hydrophobic Coatings Prepared by RF Magnetron Sputtering of PTFE. *Plasma Process. Polym.* **2010**, *7*, 544−551.

(47) Tripathi, S.; Haque, S. M.; Rao, K. D.; De, R.; Shripathi, T.; Deshpande, U.; Ganesan, V.; Sahoo, N. K. Investigation of optical and microstructural properties of RF magnetron sputtered PTFE films for hydrophobic applications. *Appl. Surf. Sci.* **2016**, *385*, 289−298.

(48) Gremaud, R.; Broedersz, C. P.; Borsa, D. M.; Borgschulte, A.; Mauron, P.; Schreuders, H.; Rector, J. H.; Dam, B.; Griessen, R. Hydrogenography: An Optical Combinatorial Method To Find New Light-Weight Hydrogen-Storage Materials. *Adv. Mater.* **2007**, *19*, 2813−2817.

(49) Vargas, W. E.; Rojas, I.; Azofeifa, D. E.; Clark, N. Optical and electrical properties of hydrided palladium thin films studied by an inversion approach from transmittance measurements. *Thin Solid Films* **2006**, *496*, 189−196.

(50) Palm, K. J.; Murray, J. B.; Narayan, T. C.; Munday, J. N. Dynamic optical properties of metal hydrides. *ACS Photonics* **2018**, *5*, 4677−4686.

(51) Setayandeh, S. S.; Webb, C. J.; Gray, E. M. Electron and phonon band structures of palladium and palladium hydride: a review. *Prog. Solid State Chem.* **2020**, *60*, No. 100285.

(52) Pivak, Y.; Gremaud, R.; Gross, K.; Gonzalez-Silveira, M.; Walton, A.; Book, D.; Schreuders, H.; Dam, B.; Griessen, R. Effect of the Substrate on the Thermodynamic Properties of PdH$_x$ Films Studied by Hydrogenography. *Scr. Mater.* **2009**, *60*, 348−351.

(53) Pivak, Y.; Schreuders, H.; Slaman, M.; Griessen, R.; Dam, B. Thermodynamics, Stress Release and Hysteresis Behavior in Highly Adhesive Pd−H Films. *Int. J. Hydrogen Energy* **2011**, *36*, 4056−4067.